Optimizing chloride-capped TiO_2 electron transport layer in planar n-i-p hybrid perovskite solar cell

Bachelor Thesis

Jan Willem Hulsebos

S2020432

Photophysics & Opto-Electronics

Rijks Universiteit Groningen

Date: 22-01-2018

First Supervisor: Prof. Dr. M.A. (Maria Antoinetta) Loi

Second supervisor: Prof. Dr. L.J.A (Jan Anton) Koster

Daily Supervisor: Sampson Adjokatse, MSc

Contents

Abstract

This thesis investigates the n-i-p planar hybrid perovskite solar cell of structure glass-ITO / compact TiO_2-Cl / $(FAPbI_3)_{0.85}(MAPbBr_3)_{0.15}$ / spiro-OMeTAD / Au. The main focus is on the investigation of the TiO_2-Cl nanocrystal electron transport layer. In particular, the influence on the solar cell performance of varying the type of dispersion solvent used, the thickness of the layer and dispersion concentration is investigated. It has been found that using hydrous MeOH instead of anhydrous MeOH as co-solvent for dispersing the nanocrystals decreases the average PCE by 4.32%. Then, by increasing the TiO_2-Cl layer thickness from 22 nm to 44 nm increases the average PCE with 5.31%. Additionally, decreasing the TiO_2-Cl dispersion concentration from 20 mg/mL to 15 mg/mL in Chloroform:MeOH solvents increases the average PCE by 0.74%.

Keywords: TiO_2-Cl nanoparticles, MeOH solvent, Chloroform solvent, n-i-p hybrid planar perovskite, ITO, Au, spiro-OMeTAD, mixed-halide, mixed-cation, FAMAPbIBr, ETL layer dependence, ETL dispersion solvent dependence, ETL concentration dependence.

General Introduction

The 2015 United Nations Climate Conference in Paris led to a global agreement to reduce the extent of climate change. The key goal of this Paris agreement is to limit global warming to a maximum of 2°C increase compared to the global temperature in 1990. Global warming is largely caused by an increase of CO_2 concentration in the atmosphere, which is released as a product from burning fossil fuels. Thus, an important pathway toward achieving the Paris agreement goal is reducing the fossil fuel use. Some major areas in which these fuels are used are electricity production, industry, and the transportation sector. In the last decades, many alternative renewable energy sources, which could replace fossil fuels, such as wind turbines, geothermal water heating, biomass fuel, hydroelectricity and photovoltaics, have been developed. This last technology is very promising as the annual potential of solar energy has been estimated by the U.S. Energy Information Administration to be 1.500-50000 EJ, several times larger than their reported 2015 annual global energy consumption of 606 EJ[1]. Therefore, the potential of photovoltaic energy conversion is very promising to help reaching the goals of the Paris agreement.

The most widely used photovoltaic system, from now on termed solar cell, is the single- and multicrystalline silicon solar cell. The state of the art verified efficiency stated by the IEEE Spectrum of the former is 25.2% and for the latter is 21.9% [2]. This reflects the ratio of useable power over incident power. These solar cells are currently widely available for home-owners and companies alike due to subsidies and large price drops over the last decades. Even though the price of solar cells has been decreasing steadily in the last years, the interest in developing more efficient or more versatile solar cells has been very high. From the 1980's onward, research has been focused on cheaper materials such as thin films. From the several types of thin films investigated, namely, inorganic, polymer based, and quantum dots, the most promising, which appeared only very recently, are the organic-inorganic hybrid perovskite-based thin film.

In this thesis, the research into this organic-inorganic hybrid perovskite solar cell is presented. The goal of this research is to optimize the solar cell performance by investigating and varying the deposition parameters of the electron-extraction layer.

Hybrid Perovskite Solar Cells

General structure of organic-inorganic hybrid perovskites and composition

The thin film solar cell used in this experiment is based on a particular type of absorbing material: the organic-inorganic hybrid perovskite. The word perovskite relates to a general structure with the formula ABX_3, where in our specific case A is an organic cation, B is a metal cation, and X is a halide anion [4,5]. It has been shown by many research groups that the type of structure and its symmetry determine the electronic properties and stability of the perovskite [3,4,6]. The ideal cubic structure illustrated in figure 1, has good electronic properties due to its "high degree of ionic bonding" [4]. Green *et al.*, explain that the amount of structural disturbance from this ideal structure is described by a tolerance factor t and octahedral factor μ[3]. They illustrate that the tolerance factor t is defined as the ratio of the distance of the A cation to the

X anion and the distance of the B cation to the X anion. Furthermore, they define μ as the ratio of the B cation to the X anion which they argue is directly related to the BX_6 structure in the perovskite[3]. According to Chen *et al.*, cubic structures occur for halide perovskites when *t* is between 0.85 and 1.11[4]. Furthermore, they investigated that for halide perovskite formation to occur and BX_6 to be stable, μ must be above 0.442 and when A is a small monovalent cation, such as methylamonium (MA) or formamidinium (FA), as used in this experiment, 3D symmetry is achieved [4].

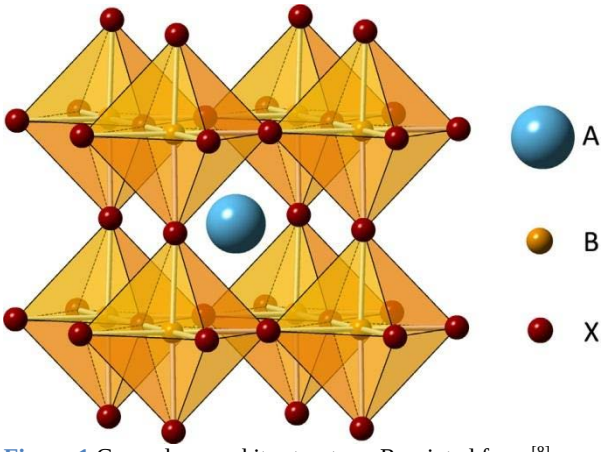

Figure 1 General perovskite structure. Reprinted from [8].

Numerous studies argue that the role of the A cation is to neutralize the total charge of the perovskite and its size affects the stability of the perovskite structure and also its electronic and optical properties[4,6,7,10,11]. According to Chen *et al*, the A cation has weak electronic interaction with the B and X components because of the negligible overlap of its electronic orbitals with the BX_6 octahedral[4]. Furthermore, according to Jung *et al.,* and Chen *et al.,*, the A cation has no direct influence on the valence band maximum and conduction band minimum of the perovskite which in turn influence the bandgap the material [4,9]. However, from several studies which will be mentioned at the end of this section, its size can affect the symmetry of the structure. They illustrate that when one chooses A with a relatively large ionic radius, $t \to 1$, it leads compression and tilting of the internal lattice structure. This leads to distortions of the bond length and angle between B and X making the structure unstable. Consequently, this altering of B-X bonds in the BX_6 structure has the greatest impact on tuning the bandgap energy of the material. Thus, as concluded by multiple papers, the choice of A cation has a direct influence on the bandgap and stability of the perovskite structure [4,6,7,10,11].

Recently, several researchers have investigated the use of mixing FA and MA in the A position in the perovskite structure. In order to illustrate its beneficial electronic and optical properties, it is important to include several experimentally established parameters of $FAPbI_3$ and $MAPbI_3$ separately as these two perovskites have been investigated thoroughly.

First, Chen *et al.*, Calió *et al.*, and Grätzel argue that the asymmetry of the FA and MA cations results in "increased carrier lifetime [and] enhanced charge carrier separation"[4]. Chen *et al.*, and Grätzel explain that this asymmetry prevents the presence of an "inversion center"[4] causing the B cation to migrate in the BX_6 structure[4,13]. In effect, they illustrate that internal electrical polarization occurs [4]. They argue that this causes a large dielectric constant and

ferroelectric domains in the perovskite [4,13]. This results in an internal electric field that assists in separating photo-excited charge carriers[4,5].

Additionally, Bakr *et al.*, and Jeon *et al.*, argue that incorporating MA into an FA based perovskite leads to a more uniform crystalline perovskite as $FAPbI_3$ alone has an irregular morphology [14,15]. The morphology of the surface and grain sizes of the crystals of the perovskite influence largely the performance of the fabricated solar cells[8,14]. Furthermore, Marinova *et al*., show that including a small amount of the precursor MAI leads to better device performance [8].

Furthermore, adding FA to the perovskite extends the absorption range with about 40 nm and makes the perovskite structure more stable [3,15,16]. The much used $FAPbI_3$ perovskite has been found to have bandgap of 1.48 eV with an absorption edge of 840 nm[4,5,11,15]. This window of absorption is about 40 nm wider than $MAPbI_3$, which has a bandgap of 1.5-1.6eV and an absorption edge of approximately 800nm [4,5,11,15]. This leads to an increase of J_{SC} without a large loss of the V_{OC} [4,11]. This has been found to be caused by FA's larger ionic radius, which increases the tolerance factor, thereby reducing the bandgap [4,9,15]. Furthermore, as the tolerance factor is increased, the structure becomes more symmetrically cubic than with solely MA making it more stable [3,15,16].

Lastly, the charge collection efficiency of the device is enhanced. Jeon *et al.*, argue that incorporating FA leads to an increase of the valence band level of the perovskite, bringing it closer to the HOMO of the spiro-OMeTAD[15]. This decreases the energy offset making hole extraction more efficient [15]. Furthermore, they found that $FAPbI_3$ has a hole diffusion length of 813 nm whilst $MAPbI_3$ has a diffusion length of 90 nm[15]. Furthermore, they found an electron diffusion length for $FAPbI_3$ and $MAPbI_3$ of respectively 177 nm and 130 nm [15]. The diffusion length is "the average distance that can be covered by carriers before they recombine" [13]. Therefore, the addition of FA could increase the hole extraction efficiency in particular[15], and carrier collection efficiency in general [11,15,17].

Properties of B cation and X anion

As already briefly mentioned, it has been argued by several studies that the valence and conduction band of the perovskite come mostly from the BX_6 octahedral [4,7,11]. Thus, the choice of B cation and X anion largely determines the bandgap of the perovskite. This in turn determines how many photons the solar cell can absorb which partially determine the performance of the solar cell.

As discussed by Chen *et al.*, Yin *et al.*, and Gao *et al.*, the valence band maximum (VBM) of the perovskite is formed by the "antibonding hybrid state between"[4] the 6*s* electronic orbital of B partially and the X *p* orbital mainly[4,7,11]. They also argue that the conduction band minimum (CBM) is formed by the unoccupied hybrid B *p* orbitals and X *p* orbitals which allow more electron occupation than the regular *s* states[4,7,11]. Therefore, there is a higher density of states in the CBM. Yin *et al.*, show that as the *s* orbitals below the VBM are occupied and do not lose their electrons in halide perovskites, the *p-p* transition is possible upon photo-induced excitation which they argue is stronger than *p-s* transition[7]. Therefore,

according to the three mentioned research groups, a higher density of states in the CBM and the *p-p* transition makes the perovskite a direct bandgap material.

Consequently, the use of mixtures of iodide and bromide can be used to tune the bandgap and make the perovskite structure more stable. It has been found by Chen *et al.*, that iodide and bromide based perovskites have a different bandgap[4,16]. This is a result of changing the bonds between the B cation and X anion due to the difference in ionic radii as already discussed [6]. Chen *et al.*, explain that the addition of bromide, which has a smaller radius than iodide, will "induce a compressive stress on the Pb-I bonds, causing structural distortion that leads to the observed bandgap increase"[4]. It has also been found that this mixture increases the perovskite stability to moisture and temperature [16]. Furthermore, several papers show that devices made with mixed X anion show an increased charge carrier diffusion length compared to a single species anion [9,10,16]. Thus, these papers showed that a mixed anion leads to a more stable structure and longer diffusion lengths.

Material Properties of hybrid perovskites

Hybrid perovskites have strong light-absorption properties and high and balanced charge-carrier mobility [4,5]. They also exhibit ambipolar characteristics and have a direct band gap [5,11]. Furthermore, these materials show instant photo-induced charge carrier generation[4] and slow charge recombination [7,9,10,11]. Additionally, Chen *et al.*, demonstrated bandgap tuning via compositional variation and formation of multi-dimensional structures[4]. Thus these materials are very versatile.

Next to the good optical and electrical properties, perovskite solar cells have fabrication advantages as they are solution processable. A variety of architectures and processing techniques have been reported which can easily obtain an efficiency of 15% [4]. One of those techniques, such as single-step solution deposition, can easily be used not only at the laboratory level but can also be upscaled. Therefore, the large interest in these solar cells is due to easy fabrication techniques and large efficiency [4,19].

History and development of hybrid perovskite solar cells

The development of the hybrid perovskite-based solar cells given here is based on accounts of Grätzel[13], Green *et al*[3], and Chen *et al*[4]. The perovskite was initially used as dye-absorber placed on a TiO_2 mesopourous structure in a "liquid electrolyte-based dye-sensitized solar cell (DSSC)" [4]. In this class of solar cells, the dye absorbs photons from which an exciton is created which eventually separates into free charges. The electrons are then transported to a TiO_2 layer, which it envelops. The holes are transported by the liquid electrolyte, which also provides new electrons for the dye/TiO_2 layer. The TiO_2 and liquid electrolyte materials thereby act as selective contacts through which the charge carriers are extracted from the device. They are usually respectively termed as electron transport layer, ETL, and hole transport layer, HTL. It was found that increasing the amount of the perovskite dye increased the device efficiency [3,4]. This resulted in efficiencies of 3.8% in 2009[35] and 6.5% in 2011[36]. However, the device stability was poor due to the fast dissolution of the perovskite in the liquid electrolyte [3,4,5]. An advancement was made by replacing the liquid electrolyte with the solid state HTL, namely, spiro-OMeTAD [3,4,5,13]. From these two major developments, several other developments in the

device structure, and perovskite-, ETL-, and HTL-materials have been made which led to the increase of efficiency from 9.7%[38] in 2012 to 22.7% most recently[20].

Device architecture

The device architecture used in this experiment is a planar n-i-p structure. The word planar refers to the stacking of compact layers to form the solar cell. In contrast, in a mesoporous structure the ETL layer extends into the perovskite layer. This allows the perovskite to have a shorter charge carrier diffusion length as the generation of free charge carriers is close to the junction at which carriers are extracted. Additionally, in a n-i-p structure, the photons enter via the n-type layer before entering the active, intrinsic, layer. In a p-i-n structure, also called inversed structure, the photons enter the solar cell via the p-type layer first. The choice of using which structure depends partially on which type of materials is used.

Solar Cell Theory

Working principle of solar cells, properties of materials and J-V characteristics

Firstly, the fabrication of a solar cell requires a semiconducting material in which an electron can be excited into a higher energy state when it absorbs a photon with sufficient energy, leaving behind a hole. The energy of the excited electron must be equal to or more than the energy difference between the higher and lower energy state in order to prevent the electron from recombining with the hole in the lower energy band. Secondly, it requires an internal electric field to separate and collect the charges. This is usually provided by a p-n junction like in silicon solar cells or p-i-n junction like in the perovskite solar cell.

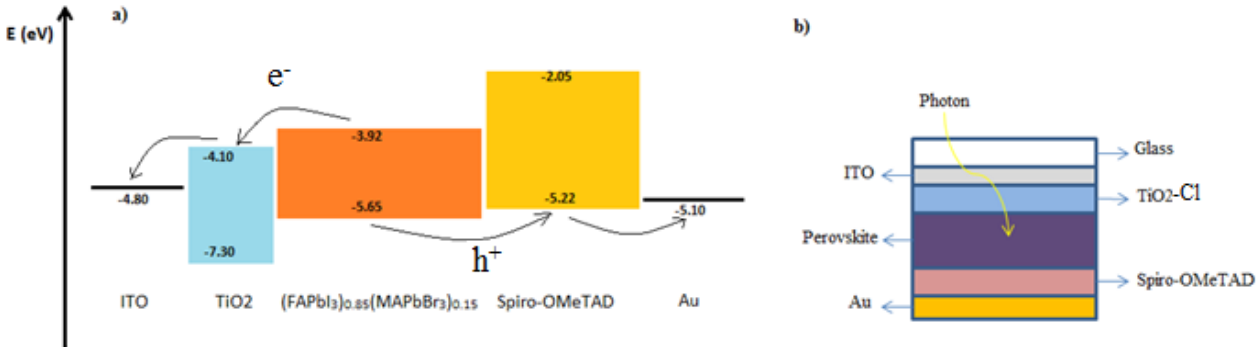

Figure 2 Figure a) illustrates the band diagram of perovskite solar cell with approximate and relevant valence band and conduction band values, which are taken from [5,7,13]. Figure b) shows the planar structure of solar cell.

Using both figure 2a and 2b, one can illustrate the working principle of the planar n-i-p perovskite solar cell used in this experiment. The p- and n-type materials required to spatially separate the photo-induced free charges through an electric field are represented by the HTL, spiro-OMeTAD, and ETL, TiO_2-Cl, layers respectively. Photons pass through the glass/indium-doped tin oxide (ITO) into the active absorber material, the perovskite. If the photons interact with the absorber material, they can excite an electron to the conduction band of the perovskite and the hole goes to the valence band. These two bands are illustrated in figure 2a by the highest and lowest energy of the material respectively as indicated. The electron (hole) travels through

the active material to the ETL (HTL) layer and eventually to the electrodes to be extracted into an external circuit to be used. It has been found by many studies that the inclusion of these layers improve charge selectivity and lowers charge recombinations which influences the solar cell performance [4,22]. Several parameters determine whether the electron and hole will be successfully separated and collected at the electrodes in order for the solar cell to create a current. These will be discussed later in this thesis.

Structure and optical properties

To investigate the structure of the perovskite, an X-ray diffraction, XRD, can be used. This technique is based on Bragg's law. X-ray light is directed at the sample and when this law is upheld, constructive interference can occur between the diffracted beams reflected from different planes in the crystal structure. These waves can then be detected. The University of Sheffield website explains that "the positions of these reflections tell us about the inter-layer spacings of atoms in the crystal structure" [32]. Thus, they explain that the position and peak of the reflections quantify the "crystallinity of a sample, the crystal structures and their lattice parameters, [and] crystallite size"[32] for example.

J-V characteristics

The following discussion and figures are based on the account by Spiers[37]. The performance of a solar cell is characterized by a J-V curve. This is its current density (J) behavior, determined as the current (I) divided by device area (A), plotted against an applied voltage (V). The dark J-V curve, under no illumination, is shown in figure 3a. The connected line is a linear plot and the dotted line is logarithmic plot. The logarithmic plot is used to analyze the different resistances in the cell. For voltages close to 0 V, regions 1 and 2, the curve is "dominated by the symmetric shunt current resulting from the finite shunt resistance"[37]. Honsberg and Bowden argue that a low shunt resistance decreases the current through the cell[30]. It provides an alternate, parallel, pathway for the current which then will not flow through the solar cell [30]. Qi *et al.*, illustrate that a low shunt resistance causes current loss through pinholes or trap states which can be improved by creating a good morphology of all the layers and interface between the layers [31]. Pinholes can cause direct contact between the ETL and HTL thereby increasing the chance of recombinations. At larger voltage, region 3, the diode-like behavior of a solar cell is illustrated until the current is limited by series resistance, region 4[37]. Honsberg and Bowden illustrate that series resistance can be caused by the resistance due to the movement of charge carriers through the bulk of the layers, the contact resistance between the interfaces of the materials, and the resistance of the top and back contacts [30].

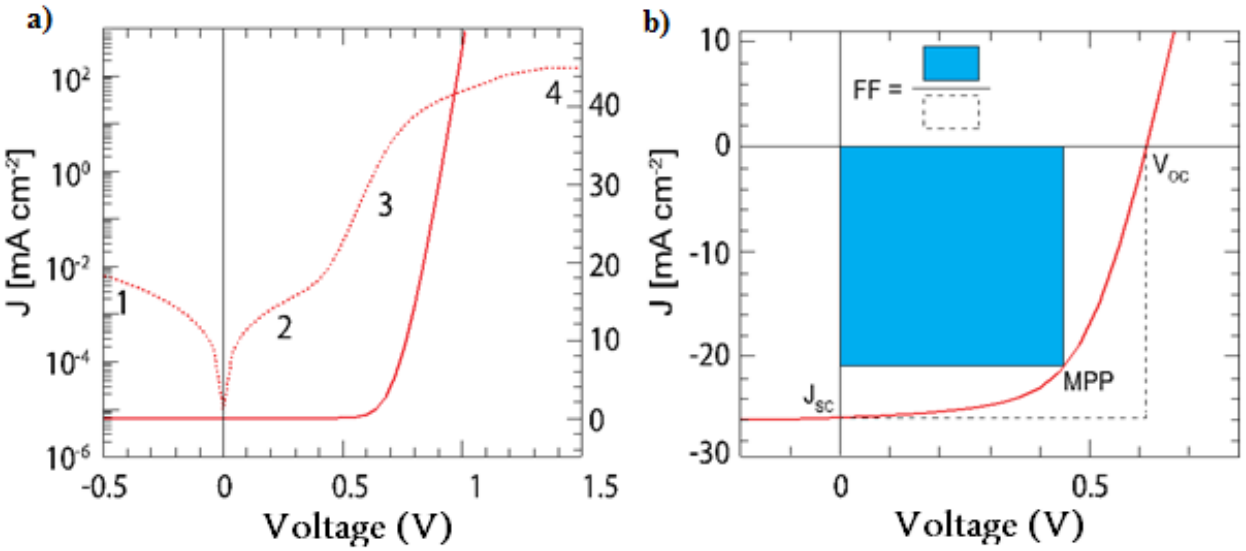

Figure 3 Meaning and interpretation of dark and light J-V curves. A dark J-V curve in both logarithmic and linear scale is given in figure a) and an illuminated J-V curve is given in figure b). Taken from [37].

When the cell is under illumination, the "photo-induced current shifts the entire [dark] curve downwards"[37], as shown in figure 3b. Figure 3b illustrates some important parameters of an illuminated solar cell from which the efficiency of the device is calculated. First, the short circuit current density, J_{SC}, is defined at 0 Volts. According to Honsberg and Bowden, at this point almost all photo generated current can be extracted and it is the maximum current density of the solar cell [30]. They argue that the J_{SC} is influenced by the series resistance and depends on the diffusion length of the charge carriers in the active material [30]. Second, Honsberg and Bowden explain that when the circuit is broken, the photo-induced charge carriers are not extracted and the number of electrons on the n-type material and the number of holes on the p-type material will increase due to the electric field from the p-n junction[30]. They explain that this accumulation of charges will induce an electric field opposite in direction to the p-n junction field thereby reducing the net electric field which increases the diffusion current across the junction[30]. They argue that the external voltage required to balance the light-generated current and this forward bias diffusion current, leading to zero net current, is called the V_{OC}[30]. This point is also shown in figure 3b at $J = 0$. Qi *et al.*, argue that the V_{OC} is influenced mostly by non-radiative recombinations which can occur due to current leakage, trap states or low shunt resistance [31]. Therefore, the V_{OC} can be considered as a measure of the amount of non-radiative recombinations [30].

The point where the solar cell delivers the maximum power is called the maximum power point (MPP) in figure 3b and is an indication for the efficiency of the solar cell. The current density and voltage at this point are called J_{MPP} and V_{MPP}. The PCE is defined as "$PCE = \frac{J_{SC}V_{OC}FF}{P_{light}}$"[37] . Here FF is the fill factor defined as "$FF = \frac{J_{MPP}V_{MPP}}{J_{MPP}V_{OC}}$"[37] or, as shown in figure 3b, as a measure of the squareness of the J-V curve. Spiers argues that the FF is "determined by the competition between charge extraction and recombination"[37]. This is influenced by the quality of the junction and the crystallinity of the layers. Furthermore, according to Qi *et al.*, the dominant

factor influencing the FF is the series resistance [31]. Thus, the PCE is an indication of the performance of a solar cell.

In order to compare devices, a certain standard illumination must be upheld. In general, a standard 1000 W/m^2, or 100 mW/cm^2, AM1.5G solar spectrum is attained with an illumination source. This is the spectrum of the sun at the surface of the Earth after being filtered by 1.5 atmospheric volume. AM0G is in space and AM1G is when the sun shines directly from the zenith. Thus, the PCE is calculated as $\frac{MPP\ (\frac{mW}{cm^2})}{100mW/cm^2} \times 100\% = MPP(\%)$.

Choice of ETL and HTL materials, dopants and solvents

According to Qin *et al*, the choice of ETL and HTL materials has a direct effect on the V_{OC} and thereby efficiency of the solar cell. They argue that the V_{OC} is "directly proportional to the difference between the lowest unoccupied molecular orbital (LUMO) of the [p-type] and the highest occupied molecular orbital (HOMO) of the [n-type material]" [25]. Furthermore, charge extraction is boosted with lower energy offset between the ETL/perovskite and HTL/perovskite layers [23]. Therefore, the energy levels between all layers must be optimized to reduce recombinations, energy loss, and charge accumulation at interfaces. Additionally, Sherkar *et al.*, argue that doping of the HTL and ETL layers increases their conductivity and the internal electric field strength resulting in more efficient charge carrier extraction from the active layer to the contacts [23]. However, it has been observed that doping the HTL and ETL makes the device more unstable [5].

Spiro-OMeTAD

In general, the HTL must have "a low electron affinity" [14]. Also, Bakr *et al.*, explain that its HOMO should be higher than the valence band of the perovskite but as close to it as possible for efficient hole extraction [14,26]. Even though numerous HTL materials have been investigated, the organic small molecule spiro-OMeTAD is one of the few which have resulted in efficiencies of over 20%[27]. Therefore, in this study, the spiro-OMeTAD is used as HTL material.

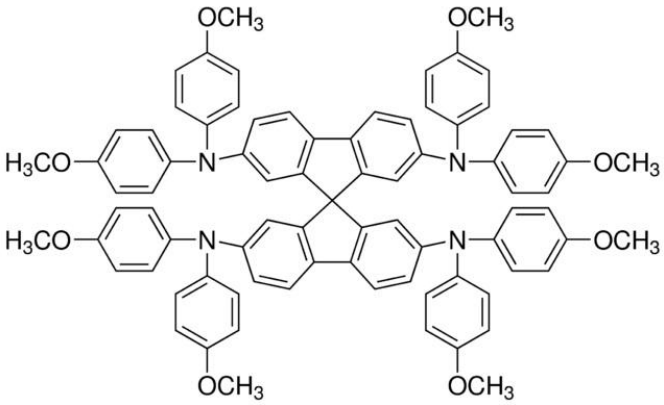

Figure 4 The structure of pristine spiro-OMeTAD [4].

The chemical structure of spiro-OMeTAD is displayed in figure 4. Several studies have shown that it has a suitable bandgap and HOMO level compared to the perovskite which enhances hole

extraction efficiency and helps to minimize recombination [5,14,21]. It has been found that the HOMO of the spiro-OMeTAD and the valence band of $FA_{0.85}MA_{0.15}PbI_{2.55}Br_{0.45}$ respectively is -5.22 eV and -5.65 eV which is an offset of only 0.43 eV [5,21].

However, as Bakr *et al.,* Ameen *et al.,* and Xi *et al.,* show, like most organic HTL's in their pristine form, spiro-OMeTAD has a relatively low conductivity, which is due to large intermolecular distances[14,21,27]. Consequently, to improve its charge carrier mobility and hole collection efficiency it has been chemically doped in numerous studies [4,5,8,14,21,27,28]. In this experiment, the "p-type dopant or ionic additives"[27] Li-TFSI ((Lithium Bis (trifluoromethylsulfonyl) amine) and tBP (tert-butylpyridine) are used [27]. Xi *et al.,* argue that the use of tBP helps in the formation of a homogeneous spiro-OMeTAD layer, improves charge selectivity and transport, and stabilizes the HTL[27]. However, they also argued that it is uncommon to use only tBP as dopant as it is a polar solvent with good perovskite solubility thereby threatening to erode the perovskite[27]. Therefore, they have found that using a mixture of a small amount of tBP with Li-TFSI might lead to a more uniform film and better performance[27]. Furthermore, Xi *et al* argued that using Li-TFSI reduces charge transport resistance, improves hole extraction efficiency, and increases stability in the spiro-OMeTAD [27].

TiO_2-Cl nanocrystals

The compact TiO_2-Cl nanocrystal layer acts to minimize the recombination of holes at the front electrode and extract electrons from the perovskite and guide them to the electrode [4,5]. Its conduction band alignment with the perovskite is important as an energy mismatch can give an offset for the electron injection [18] influencing the performance of the device. The approximate value of the conduction band of compact TiO_2-Cl and $FA_{0.85}MA_{0.15}PbI_{2.55}Br_{0.45}$ respectively has been measured to be -4.10 eV and -3.92 eV [5,21]. This is an energy threshold of 0.18 eV, which is quite low. Therefore, one would not expect much mismatch losses. Furthermore, Wiranwetchayan *et al.,* illustrate that the choice of dispersion solvents can affect the opto-electronic properties of the TiO_2-Cl nanocrystals [29]. This is related to the properties of the solvents used like "boiling point, dielectric constant and viscosity" [29]. The choice of these dispersion solvents is given later in this thesis.

Importance of precursors, solvents, and annealing

For optimum solar cell performance, a uniform film morphology, good interfaces between layers and crystallinity of the materials must be attained. Even though the details of all the materials used is provided later in this thesis, the importance of investigating the effect of the materials and processes used is given here.

Sherkar *et al.,* show that non-radiative recombinations predominantly affect the efficiency of the device and mostly take place in trap states introduced by defects or impurities at interfaces [23]. Thus, as has been shown and argued by many studies, a dense and uniform film, with few pinholes and defects, good crystallinity, large grain sizes and appropriate thickness are required to enhance the $V_{OC,}$ FF and J_{SC} [10,24]. Marinova *et al.,* argue that the crystal growth and perovskite structure formation can be controlled by the choice of solvents and annealing[8].

Additionally, several papers indicated the importance of the deposition method, precursor materials and amounts, and type and amount of solvents for achieving a uniform film and interfaces[4,8,13].

It has been found by Chen *et al.*, that the stoichiometry of the precursors have an effect on the resulting optical and electrical properties of the perovskite[4]. Marinova *et al.*, argued that when using "non-stoichiometric precursor solution, with PbI_2 in excess, the unreacted PbI_2 improves the crystallinity of the perovskite film"[8] as this apparently leads to bigger perovskite crystallites after annealing [8]. This reduces grain boundary surface and thus less area for defects to occur and thereby less non-radiative recombination [8,16,23].

Moreover, Grätzel and co-workers and Chen *et al.*, argue that the reason for dissolving the precursors of the perovskite is to control crystal growth and the nucleation of the perovskite which are the two main steps in achieving a uniform crystal [4,13]. In controlling the crystal growth the solubility, boiling point, viscosity and interaction between precursor materials and solvents must be taken into account [4]. Chen *et al.*, argue that using mixed solvents influence the interaction between the materials and thereby have a large effect on film quality [4].

Hysteresis

In all our devices, a measure of hysteresis has been observed. This phenomenon is the different current density response to an applied voltage depending on the direction and speed of the voltage sweep over the device. Grätzel argues that this can lead to a large overestimation of the performance of the device [13]. The exact cause of this phenomenon is still not agreed upon. However, there are several theories in the literature, three of which will be briefly discussed here.

First, some studies report that large defect densities in the device may result in large density of trapped carriers which cause this hysteresis effect [4,9,19]. These defect densities can be suppressed by creating large crystals as this reduces the grain boundary surface which is the main site for trap states according to several studies [4,9,19].

Second, it is argued by Chen *et al.*, and Correa Baena *et al.*, that as MA and FA are non-spherically symmetric, ferroelectric domains are created in the perovskite which polarizes the charged species in a certain direction[4,22]. Thus the perovskite material has a certain dipole ordering and consequent polarization. Then, they argue that when an external electric field is applied, an external voltage, the polarity in the device is disturbed. The amount of disturbance depends on the direction and intensity of applied electric field. Consequently, they show that the pathway of charge carriers through the perovskite upon photo-excitation will be influenced by this polarity. This polarity-voltage dependence thereby influences how well the charges are extracted from the device. Subsequently, they argue that this effect results in the J-V hysteresis [4,22].

Third, Chen *et al.*, Correa Baena *et al.*, and Sherkar *et al.*, argue that the migration of iodide ions can be a reason for the hysteresis in the J-V curves[4,22,23]. They claim that under an applied voltage, some excess iodide ions could migrate through the active layer[4,22,23]. These mobile

ions could then accumulate at interfaces which then shield the internal potential of the perovskite[4,22,23]. Next to that, they can serve as trap states as Chen *et al.*, argue they can act as defects states where charge recombination can occur [4]. Thus, they argue that this effect influences the efficiency of charge extraction [4,22,23].

Experimental Methods

Material details, fabrication and characterization

The cleaning procedure, deposition method, precursor materials, ETL/HTL materials, solvents, and annealing are discussed below. As already mentioned, these methods have a large influence on the performance of the device as they influence the eventual morphology and crystallinity of the layers and the interfaces between the layers and thereby the opto-electrical properties. The parameters for all these methods have been optimized by Sampson Adjokatse during his PhD research.

Cleaning procedure

Before using the ITO-glass substrates they are cleaned. This is a sequential procedure starting with manual scrubbing with nitrile gloves in ultraclean water mixed with soap and kept at 100°C. This is to remove any spikes and leftover oil on the ITO surface. Then, the substrates are sonicated in ultraclean water for 20 minutes, replacing the water after 10 minutes. Subsequently, the substrates are sonicated for a total of 20 minutes in acetone, replacing the acetone after 10 minutes with new aceton. Then they are sonicated once in propanol for 10 minutes. The substrates are dried using an N_2 gun and annealed in an oven for 10 minutes at 140°C. Lastly, they are treated with UV-ozone for 20 minutes. This is to remove any organic material still left on the substrates.

Solvent engineering

Both Chen *et al.*, and Calió *et al* investigated the addition of chlorobenzene during the single-step deposition processing of the perovskite material. They found that exposing a wet film to a nonpolar organic anti-solvent such as chlorobenzene induces a “fast crystallization process [with] fast nucleation and crystal growth”[4]. According to both studies, this results in a more homogeneous, smooth and dense polycrystalline film with large grains across the whole surface [4,5]. Thus, solvent engineering is important as one can control nucleation and crystal growth and create a good performing perovskite structure [4,5].

Thermal annealing

The reason for thermal annealing is that it “is an essential step to initiate or accelerate the reaction between the organic and inorganic species” [4]. Chen *et al.*, argue that the time and temperature of annealing determines the surface coverage and morphology of the film: “Fast annealing treatment has been reported by Saliba *et al*. for higher temperatures and shorter times to enhance device performances for planar structure devices” [4]. Thus, the annealing process

drives out the solvents and crystallizes the perovskite structure [5]. The particular annealing temperatures and times are given below since they are specific to the material.

Material fabrication and deposition

Chen *et al* and Zhou *et al* argue that the deposition method, production environment, precursor materials and composition, solvents and additives used highly influence the performance [4,12]. Therefore, it is important to detail these processes very clearly. This is done below.

Chloride-capped TiO_2

The ETL layer consists of TiO_2 chloride capped nanocrystals which are dispersed in anhydrous chloroform/methanol (Chloroform:MeOH) mixture in 1:1 volume ratio. This was done in concentrations of 15 mg/mL and 20 mg/mL. The nanocrystals are made following the procedure reported by Sargent and coworkers[34]. The layers were spincoated at 4000 rpm with an acceleration of 1000 $rpms^{-1}$ for 60 seconds. To study the thickness dependence, single and double layers were spincoated. For the single layer, the substrates were annealed at 150°C for 30 minutes on a hot plate. The double layers were spincoated with the same parameters but annealed for 2 minutes at 150°C before spincoating the second layer at the same parameters and annealed for 30 minutes.

Perovskite

The molar ratios of the precursor materials for the perovskite are the same as the molar ratios as described by Tan *et al.*,[34]. This is then added to 800 µL DMF (dimethylformamide) and 200 µL DMSO (dimethylsulfoxide) and stirred for at least 3 hours to properly dissolve the materials. The mixed-halide, mixed-cation perovskite film is fabricated using single step solution deposition in mixed solvents. This is also called the "One-Step Precursor Deposition (OSPD)"[11] where the precursors are mixed and dissolved in DMF and DMSO, in a ratio of 4:1, before spincoating on the n-type selective contact, compact-TiO_2-Cl. It has the following composition: $FA_{0.85}MA_{0.15}PbI_{2.55}Br_{0.45}$. Here FA is the formamidinium ($(NH_2)_2CH^+$) ion and MA is the methylammonium ($CH_3NH_3^+$) ion which represents the A cation in the ABX_3 structure of the perovskite in the ratio stated. The metal cation B is Pb and the halide anion X is a mixture of iodide and bromide, I^- and Br^-.

Before use, the perovskite is filtered through a 0.2 µm PTFE microfilter and spincoated in two steps. The first step is at 1000 rpm with an acceleration of 200 $rpms^{-1}$ for 10 seconds. The second step is at 4000 rpm with an acceleration of 1000 $rpms^{-1}$ for 30 seconds. Prior to the last 10 seconds of the second step, 100 µL of chlorobenzene is added as anti-solvent. The films are annealed on a hot plate at 100°C for 10 minutes to form the perovskite crystalline film [11].

Spiro-OMeTAD

The spiro-OMeTAD precursor in powder form is dissolved in chlorobenzene at a concentration of 70 mg/mL. Similarly, a concentration of 170 mg/mL of Li-TFSI in aceton-itrile is made and 1 mL of spiro-OMeTAD/CB mixture is doped with 70 µL of Li-TFSI/aceton-itrile and 20 µL of tBP. This mixture was then stirred for some time as well prior to deposition. Before use, the

doped spiro-OMeTAD is filtered through a 0.2µm PTFE micro-filter. The solution is spincoated at 3000 rpm with an acceleration of 1000 $rpms^{-1}$ for 30 seconds.

Thermal evaporation of contacts

The gold contact layers were thermally evaporated onto the spiro-OMeTAD and ITO layers. This was done under vacuum condition where the pressure varied between $1 \cdot 10^{-8} - 4 \cdot 10^{-8}\ mbar$. An initial deposition rate of 0.05 nm/s was used until a thickness of 10 nm. Then, the deposition rate increased to 0.1 nm/s and at 20 nm it increased to 0.2 nm/s until a final thickness of about 80 nm. The reason for the initially slow deposition rate is to create a homogeneous gold layer.

Measuring the J-V, structural and optical characteristics of the devices

To quantify the electrical performance of the devices, a solar simulator is used. The devices are illuminated under 1000 W/m^2 intensity of the standard AM1.5G solar spectrum. The solar cells are kept at approximately 295 K using liquid nitrogen. A thermocouple is used to measure this temperature.

In order to compare devices, the area of the cell and the spectrum and intensity of the light must be made constant for all measurements. The reason for this is because the J_{SC}, and therefore the calculated efficiency of a solar cell, depends on all three factors [30]. Therefore, before each measurement, the light intensity is calibrated. This is done using a silicon reference solar cell of known current-voltage response. All the devices were measured at a distance where the silicon cell produced a direct short circuit current between approximately 137.8 – 138.6 mA.

The device is then placed on a holder with a mask over the substrate. This is to restrict the solar cell area on which the photons impinge the materials to 0.1 cm^2. A forward and reverse bias sweep is measured. A forward sweep means that the voltage was increased from low to high voltage and reverse sweep means from high to low voltages. The dark measurement was done with steps of 0.04 V with 0.01s delay time with the voltage ranging from -2 to 2 V. The light measurements was done with steps of 0.04 V and a time delay of 0.2s with the voltage ranging from -0.2 to 1.2 V. The measurements are made using a Keithley 2400 source-meter.

The X-ray data was collected using a Bruker D8 Advanced diffractometer in Bragg-Brentano geometry and operating with Cu Kα radiation source (λ = 1.54 Å) and Lynxeye detector. X-ray photons are shot at the perovskite film and the diffracted X-rays are then collected by the detector at particular angles. During the measurement, the film rotates in order to receive good data points across the film, rather than at a single part of the film.

In order to analyse the absorption curve of the perovskite absorber, photons of a wavelength range between 500 nm and 1000 nm are directed toward the perovskite film. Then, the absorption curve of a reference glass/ITO substrate is compared with the glass/ITO/perovskite film.

The AFM images were obtained using the Bruker NanoScope V in the ScanAsyst mode.

Results & Discussion

Characterization of TiO_2-Cl

The thickness of the TiO_2-Cl nanocrystal layer is varied by spincoating a dispersion of concentration of 15 mg/mL once or twice. The thickness has been measured using a spectroscopic ellipsometer. The results are given in table 1 below with an error of 10%.

Type of layer	Thickness (*nm*)
Thicker-based	44.0±4.4
Thinner-based	22.2±2.2

Table 1 Measured thicknesses of TiO2-Cl layers deposited from precursor concentration of 15mg/mL.

From table 1, one can conclude that the double layer TiO_2-Cl is approximately twice the thickness of the single layer.

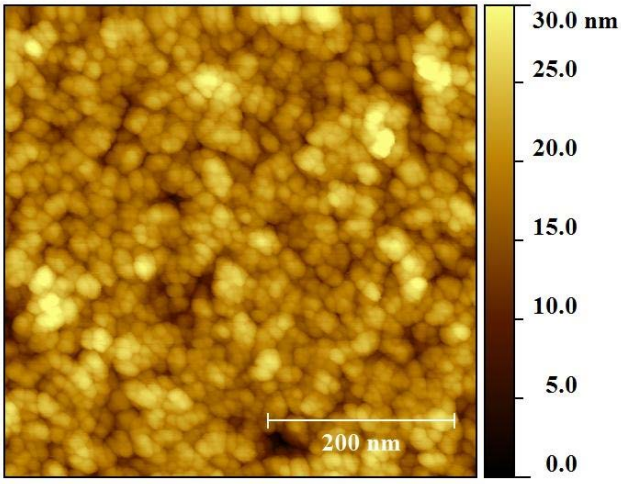

Figure 5 AFM image of a typical morphology of the TiO2-Cl nanocrystals used in this experiment.

The TiO_2-Cl nanocrystal layer morphology is measured by an Atomic Force Microscopy which is displayed in figure 5. The morphology of the layer influences the efficiency of electron extraction thereby affecting the performance of the device. The Root Mean Squared of this image is 4 nm which illustrates the smooth morphology of the layer.

Optical and structural properties of FAMAPbIBr

Figure 6a shows the absorption spectrum of FAMAPbIBr. It shows that the absorption onset of the perovskite structure is around 770 nm and extends along the visible spectrum. The absorption spectrum was measured with the perovskite directly deposited on the ITO/glass substrate. This result is comparable but slightly lower to other absorption onsets. The following example is merely used to display the different absorption onsets for different compositions of the perovskite. Yan *et al.*, used a very similar perovskites structure which reported an absorption onset of 811 nm and 832 nm for 0.8 and 1.0 part FA in FAMA [33]. The perovskite used was $(FAI)_x$ $(MABr)_{1-x}PbI_2$. Therefore, even though the comparison does not hold as this experiment uses a different ratio of I to Br, their results give a nice example of changing the absorption of the perovskite for different perovskite structures.

Figure 6b presents the X-ray diffraction spectrum of our perovskite material. The position and intensity of the peaks give information about the crystal structure and phase. By comparing the position of the peaks to an XRD spectrum made by Yan *et al*, we can say something qualitatively about the crystal structure. The main diffraction peaks in the $(FAI)_x(MABr)_{1-x}PbI_2$ of Yan *et al* shift from 14.5°, 20.3°, 24.9°, 29.0°, 32.4°, and 44.0° to lower angles for increasing *x* and are assigned to the 110,112,211,220,310,330 and 224 diffractions[33]. These numbers are Miller indices of the planes of the perovskite. From figure 6b, one can see that these main peaks are also in our XRD spectrum. Therefore, it illustrates that our perovskite forms the same reported crystal structure.

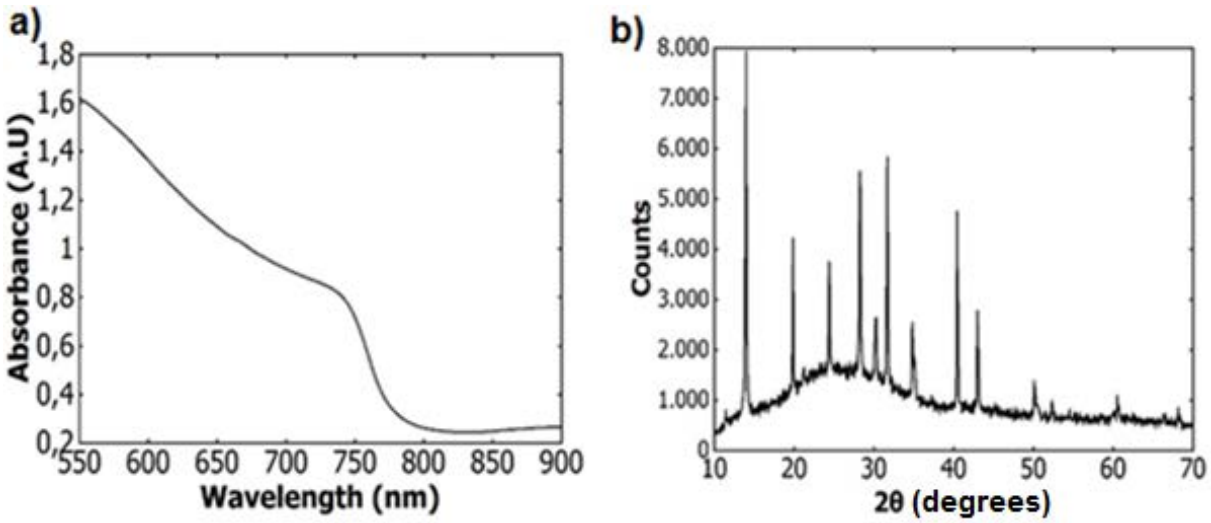

Figure 6 Figure 6 a) shows the measured Absorption spectrum and b) shows the measured XRD spectrum of the perovskite.

J-V characteristics of the solar cells

An average of the 10 best functioning solar cells has been taken for each distinct property of the solar cell unless stated otherwise. These values are presented in tables 2-4. The graphs 7-9 illustrate the dark and illuminated J-V curves of a couple of champion devices of those categories. The MPP of the devices is used as a measure for the efficiency of the devices as the incident power of the external radiation is constant.

Comparing hydrous and anhydrous MeOH dispersion co-solvent in TiO_2-Cl layer

In the following section, the terms anhydrous and hydrous cells are used to refer to the devices fabricated using anhydrous and hydrous MeOH as co-solvent in dispersing the TiO_2-Cl nanocrystals. The concentration of the TiO_2-Cl nanocrystals dispersion is 15 mg/mL and the film thicknesses have been measured to be 44.0±4.4 nm.

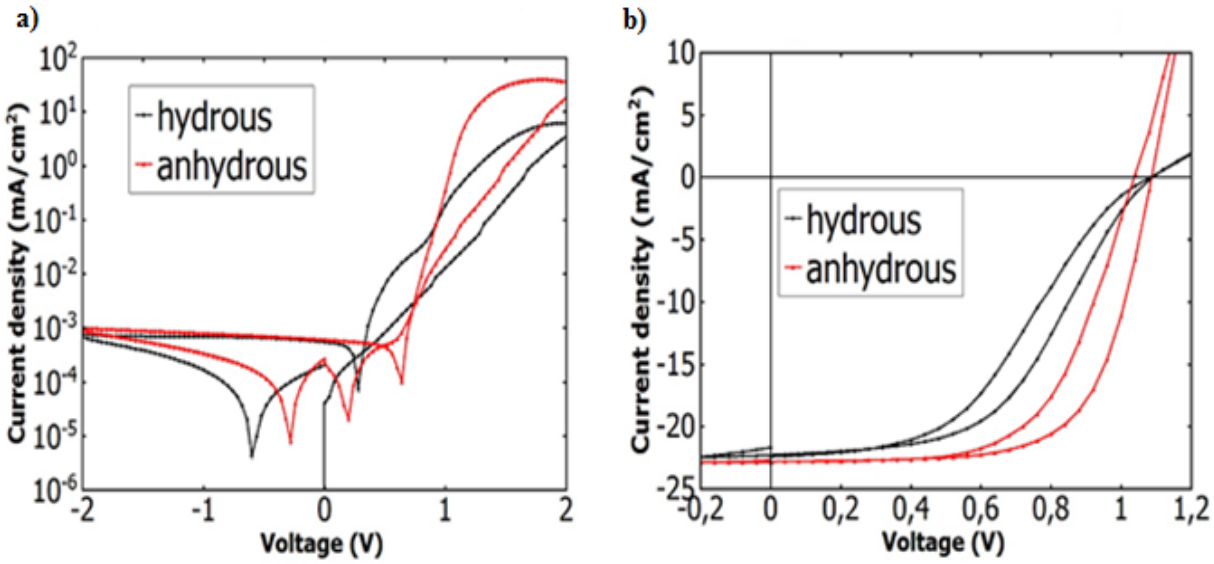

Figure 7 Figure 7a) and figure 7b) show the dark and illuminated J-V curves respectively of the champion cells for hydrous and anhydrous MeOH co-solvent of the TiO_2-Cl nanocrystal layer.

Figures 7a and 7b show the J-V characteristics of the best-performing devices based on the hydrous and anhydrous MeOH co-solvent used in the nanocrystal dispersion in the dark and under illumination. Both curves for the hydrous (black line) and anhydrous (red line) cells in figure 7a exhibit similar characteristics for voltages in the 0 to -2V range which implies that both have similar shunt resistances. However, the series resistance appears to be higher in the hydrous champion cell. This is shown in the tail of the current density toward the 2 V where a lower current density implies a higher series resistance. This is reflected in the illuminated J-V curves as shown in figure 7b where the hydrous cell exhibited lower fill factor compared to the anhydrous cell. Additionally, the champion hydrous cell shows an S-shape in its J-V curve as can be seen in figure 7b. We attribute this behavior to what Qi *et al.*, explain as an "unbalance of charge carrier mobility" [31]. That is, carriers with lower mobility accumulate in the device, leading to an additional electric field which blocks the extraction of the carriers at the electrodes[31].

Details of device	J_{SC} (mA/cm^2)	V_{OC} (V)	Fill Factor	MPP (mW/cm^2)
Hydrous				
Champion (Reverse)	22.28	1.09	0.50	12.02
(Forward)	22.39	1.08	0.43	10.40
Average (R)	22.56±0.54	1.08±0.04	0.47±0.02	11.33±0.60
(F)	22.72±0.63	1.05±0.04	0.40±0.02	9.56±0.55
Anhydrous				
Champion (R)	22.84	1.09	0.67	16.64
(F)	22.76	1.04	0.61	14.45
Average (R)	22.85±0.24	1.10±0.01	0.63±0.03	15.88±0.44
(F)	22.90±0.27	1.05±0.02	0.56±0.02	13.39±0.45

Table 2 J-V characteristics of 44 nm thick TiO_2-Cl samples of 15 mg/mL solvent concentration which are cleaned either hydrously or anhydrously. The short-circuit current, J_{SC}, open-circuit voltage, V_{OC}, fill factor, FF, and Maximum Power Point, MPP, are given.

The J-V parameters are shown in Table 2. From the table, we find that the difference in the fill factors (FF) for the reverse and forward sweeps of the champion cells are respectively 0.17 and 0.18 higher in favor of the anhydrous cells. Similarly, for the average cells, the reverse and forward fill factors are both 0.16 higher in favor of the anhydrous cells. Since the FF is related to the competition between charge extraction and recombination, we attribute the low FF in the hydrous cells to the higher rate of recombination of charge carriers and this is possibly due to higher amount of defects in the TiO_2-Cl nanocrystals. On the other hand, both the J_{SC} and V_{OC} in both voltage sweep directions are comparable for both champion cells and fall within the average standard deviation. The difference in performance, quantified by the MPP between both devices is mostly due to the difference in fill factor. On average, the MPP is 4.55 mW/cm^2, or PCE is 4.55%, higher for the reverse sweep and 4.08 mW/cm^2, or 4.08%, higher for the forward sweep in favor of the anhydrous cells. On average this is an increase of 4.32 mW/cm^2, or 4.32%.

Effect of thickness of TiO_2-Cl nanocrystal layer

In figure 8a and 8b we show the dark and illuminated J-V curves of the two champion cells based on two different thicknesses of the TiO_2-Cl layer using a dispersion concentration of 15 mg/mL. For the purpose of our discussion, we refer to the devices based on the 22 and 44 nm thick TiO_2-Cl layers as thinner-based and thicker-based devices, respectively. Unlike in the hydrate-dependent devices discussed above, the dark J-V curves in Figure 8a show a similar behavior in the 0 – 2V range and exhibits higher current density when the voltage approaches -2 V for the thinner-based device. This indicates an increase in the shunt resistance with increase in the TiO_2-Cl layer thickness. Under illumination, both champion devices exhibit similar Jsc but different Voc and FF with the device based on the thicker TiO_2-Cl layer giving better performance as can be seen in figure 8b.

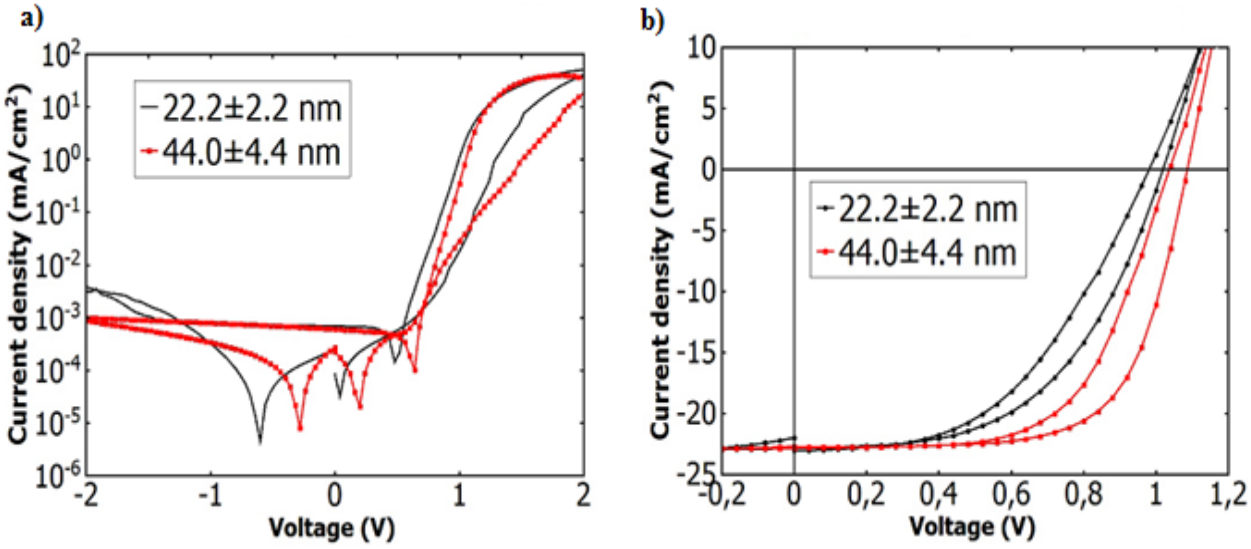

Figure 8 Figure 8a) and 8b) show the dark and illuminated J-V curve respectively for the champion cells of different thickness of TiO_2-Cl nanocrystal layer.

Details of device	Jsc (mA/cm^2)	Voc (V)	Fill Factor	MPP (mW/cm^2)
22.0±2.2 nm				
Champion (Reverse)	22.84	1.02	0.53	12.35
(Forward)	23.04	0.98	0.48	10.92
Average (R)	21.90±1.60	1.02±0.01	0.44±0.06	9.97±1.82
(F)	22.62±1.11	1.00±0.01	0.38±0.06	8.69±1.73
44.0±.4 nm				
Champion(R)	22.84	1.09	0.67	16.64
(F)	22.76	1.04	0.61	14.45
Average (R)	22.85±0.24	1.10±0.01	0.63±0.03	15.88±0.44
(F)	22.90±0.27	1.05±0.02	0.56±0.02	13.39±0.45

Table 3 J-V characteristics of TiO_2-Cl samples of 15 mg/mL solvent concentration of either thinner- (22 nm) or thicker-based (44 nm) TiO_2-Cl layers. The short-circuit current, J_{SC}, open-circuit voltage, V_{OC}, fill factor, FF, and Maximum Power Point, MPP, are given.

The J-V parameters are summarized in Table 3. The average J_{SC} of the devices from both layers are comparable to each other as they are within the average standard deviation. The average reverse sweep for the thinner-based (22 nm) devices is 20.30-23.50 mA/cm^2, well within the thicker-based (44 nm) device average of 22.85 mA/cm^2. Furthermore, the forward sweep average of the thinner-based device is within the range of 21.51-23.73 mA/cm^2. Thus, the J_{SC} of both set of devices are comparable but with the thicker-based devices being more reproducible, i.e. having a smaller standard deviation.

Regarding, the V_{OC}, the thicker-based devices showed a relatively higher value than the thinner-based devices. The reverse sweep V_{OC} of the champion cell is 70 mV higher and the forward sweep V_{OC} is 60 mV higher both in favor of the thicker-based devices. This is an average of 65 mV increase. Furthermore, for the average V_{OC} there is a difference of 0.1V and 50 mV in favor of the thicker-based devices. This is an average increase of 75mV. Consequently, since Honsberg and Bowden argue that the V_{OC} is a measure of the amount of non-radiative

recombination [30] which could be caused by defects [23], we attribute the lower V_{OC} of the thinner-based devices to interface defects. Furthermore, a thicker TiO_2-Cl layer can also suppress pinholes, which decreases recombinations and current leakage which can limit the V_{OC} as well. Another reason for an increase of recombination is limited extraction.

The FF of the thicker-based devices are higher than those of the thinner-based devices. The difference in champion FF for the reverse and forward sweep respectively is 0.14 and 0.13 in favor of the thicker-based devices. Furthermore, the average fill factor difference is 0.19 and 0.18 in favor of the thicker-based devices for reverse and forward sweep respectively. Moreover, the standard deviation of both reverse and forward sweep averages of both layered devices does not include each other's average values. Consequently, this can be due to a larger current leakage in the thinner-based devices which can be caused by pinholes. This could be due to the fact that a thicker TiO_2-Cl layer could suppress pinholes, which decreases recombinations and current leakage illustrated by high shunt resistance.

Consequently, an increase in V_{OC} and factor for the 44 nm thicker-based devices leads to an increased MPP for both the champion cells and the average of 10 cells. In forward voltage sweep, the average MPP increases by 5.91 mW/cm^2, or PCE increase of 5.91%, in favor of the thicker-based devices and in reverse sweep the increase is 4.70 mW/cm^2, or PCE of 4.70%. On average, this is an increase of 5.31 mW/cm^2, in other words 5.31%.

Effect of TiO_2-Cl nanocrystal dispersion concentration

The devices analyzed here are based on different TiO_2-Cl nanocrystal dispersion concentrations. The dispersion concentrations used for the electron extraction layers are 15 and 20 mg/mL. The layers are spin-coated twice to give thicknesses of 44.0±4.4 nm and 33.7±3.4 nm respectively. The champion devices are shown in figure 9 below.

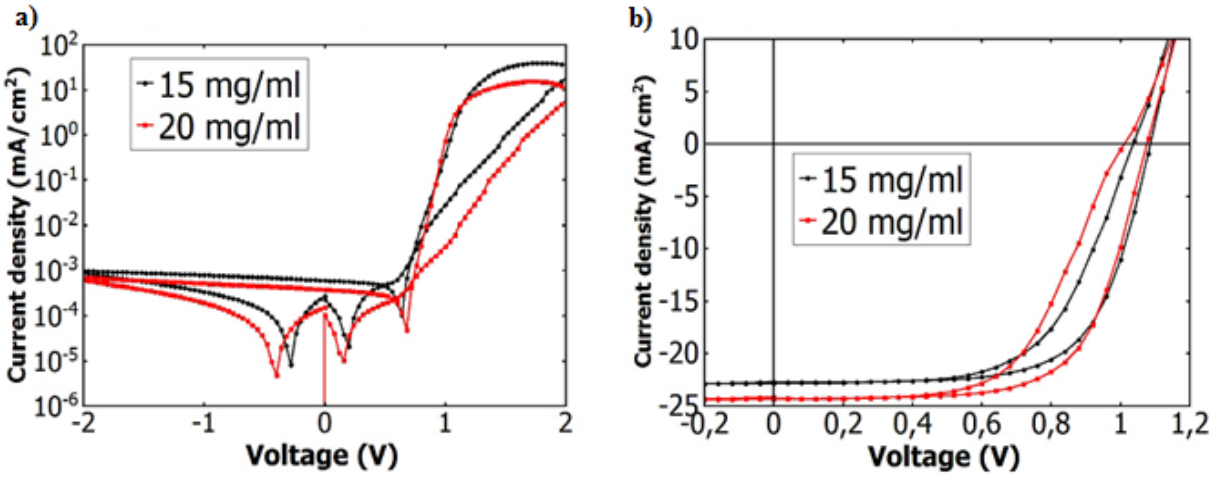

Figure 9 Figure 9a) and 9b) show the dark and illuminated J-V curve respectively for the champion cells of different dispersion concentration of TiO_2-Cl nanocrystal layer.

Figure 9a and 9b show the J-V characteristics of the best-performing devices based on 15 mg/mL and 20 mg/mL dispersion concentration in Chloroform:MeOH in both dark and under illumination respectively. The dark J-V curve in figure 9a shows that both curves exhibit a

similar current density in the range 0-2 V which implies that the devices have similar shunt resistance. However, one can see a slight increase of series resistance for the 20 mg/mL champion cell compared to the 15 mg/mL champion cell. This is illustrated by the lower current density of the 20 mg/mL devices toward 2V. The illuminated J-V curve in figure 9b shows that the 20 mg/mL device has a higher J_{SC} than the 15 mg/mL device but comparable FF and V_{OC}.

Details of device	**J_{SC} (mA/cm^2)**	**V_{OC} (V)**	**Fill Factor**	**MPP (mW/cm^2)**
15 mg/mL				
Champion (Reverse)	22.84	1.09	0.67	16.64
(Forward)	22.76	1.04	0.61	14.45
Average (R)	22.85±0.24	1.10±0.01	0.63±0.03	15.88±0.44
(F)	22.90±0.27	1.05±0.02	0.56±0.02	13.39±0.45
20 mg/mL				
Champion (R)	24.32	1.08	0.67	17.50
(F)	24.27	1.01	0.59	14.44
Average (R)	23.27±0.91	1.07±0.01	0.62±0.05	15.36±1.58
(F)	23.22±0.93	1.01±0.02	0.53±0.03	12.44±1.01

Table 4 J-V characteristics of TiO_2-Cl samples of 15 or 20 mg/mL dispersion concentration. The short-circuit current, J_{SC}, open-circuit voltage, V_{OC}, fill factor, FF, and Maximum Power Point, MPP, are given.

The J-V parameters of the champion devices and the average devices are given in table 4. We can see that the difference in J_{SC} of the champion cell is 1.48 mA/cm^2 and 1.51 mA/cm^2 for reverse and forward sweep respectively in favor of the 20 mg/mL concentration device. Additionally, the reverse and forward average J_{SC} is 0.42 mA/cm^2 and 0.32 mA/cm^2 higher in favor of the 20 mg/mL devices. However, these values fall within the average standard deviation of the devices. Therefore, one can conclude that the J_{SC} is not affected by an increase in concentration when comparing 20 devices.

Additionally, the fill factor of both the champion cells and average cells is quite comparable for both concentrations. No difference and 0.02 in favor of the 15 mg/mL champion cell and 0.01 and 0.03 in favor of the average cells for reverse and forward sweep respectively has been found. The average fill factor values fall well within the average standard deviation.

However, the V_{OC} of the 15 mg/mL champion cell is 10 mV and 30 mV higher compared to the 20 mg/mL cells for reverse and forward sweep respectively. This increase in V_{OC} is also seen in the average of 10 cells. For the reverse voltage sweep, the V_{OC} of the 15 mg/mL cells is 30 mV higher and in the forward sweep it is 40 mV higher compared to the 20 mg/mL cells. Furthermore, the average V_{OC} of the 20 mg/mL cells do not fall within the average standard. This suggests the V_{OC} of 15 mg/mL is reproducibly higher. Thus, the V_{OC} decreases when the TiO_2-Cl concentration increases from 15 to 20 mg/mL. Since the V_{OC} is a measure of the amount of non-radiative recombinations [30] which mostly takes place at defects at interfaces, a lower V_{OC} can be indicative of higher rate of recombinations which can be attributed to the increase of TiO_2-Cl concentration.

This increase in V_{OC} for a 5 mg/mL smaller dispersion concentration results in the average increase of the MPP by 0.74 mW/cm^2, or PCE increase of 0.74%. Nevertheless, the best

performing solar cell, i.e. the cell with the highest efficiency, in our experiment is the 44.0±4.4nm, 20 mg/mL solar cell with a PCE of 17.5%. However, this comparison is not fully conclusive, merely indicative, as the thickness of the 15 mg/mL and 20 mg/mL is different. Therefore, this suggests that the thickness of the different concentrations should be meticulously controlled in future experiments. This could not be done in this experiment.

Conclusion and Future Perspectives

We have successfully utilized TiO_2-Cl nanocrystals as the compact electron transport layer in the n-i-p device configuration of planar hybrid perovskite solar cell of structure glass-ITO / compact TiO_2-Cl / $(FAPbI_3)_{0.85}(MAPbBr_3)_{0.15}$ / spiro-OMeTAD / Au solar cells and have achieved a champion performance of 17.5 mW/cm^2 or 17.5%. The optimization of the ETL layers were performed by studying the effect of hydrous versus anhydrous dispersion solvent, film thickness and dispersion concentration.

We found that using hydrous MeOH as the co-solvent for the TiO_2-Cl nanocrystals dispersion results in less efficient devices. We also found that by increasing the thickness of TiO_2-Cl from 22 nm to 44 nm and by decreasing the TiO_2-Cl concentration from 20 mg/mL to 15 mg/mL the efficiency increases.

Thus, for future research, we would recommend investigating the planar n-i-p hybrid perovskite starting from a 44 nm thick TiO_2-Cl layer dispersed in Chloroform:MeOH in a concentration of 15 mg/mL. When given more time, we would investigate a lower dispersion concentration and a thicker layer as the results indicate that this may enhance the efficiency.

Bibliography

[1] U.S. Energy Information Administration, “International Energy Outlook 2017,” **2017**.
[2] IEEEE spectrum, “Interactive: Record-Breaking PV Cells,” can be found under https://spectrum.ieee.org/static/interactive-record-breaking-pv-cells, **2017**.
[3] M. A. Green, A. Ho-Baillie, H. J. Snaith, *Nat. Photonics* **2014**, *8*, 506.
[4] Q. Chen, N. De Marco, Y. Yang, T. Bin Song, C. C. Chen, H. Zhao, Z. Hong, H. Zhou, Y. Yang, *Nano Today* **2015**, *10*, 355.
[5] L. Calió, S. Kazim, M. Grätzel, S. Ahmad, *Angew. Chemie - Int. Ed.* **2016**, *55*, 14522.
[6] N. G. Park, *Mater. Today* **2015**, *18*, 65.
[7] W.-J. Yin, J.-H. Yang, J. Kang, Y. Yan, S.-H. Wei, *J. Mater. Chem. A* **2015**, *3*, 8926.
[8] N. Marinova, S. Valero, J. L. Delgado, *J. Colloid Interface Sci.* **2017**, *488*, 373.
[9] H. S. Jung, N. G. Park, *Small* **2015**, *11*, 10.
[10] G. E. Eperon, S. D. Stranks, C. Menelaou, M. B. Johnston, L. M. Herz, H. J. Snaith, *Energy Environ. Sci.* **2014**, *7*, 982.
[11] P. Gao, M. Grätzel, N. Mohammad K., *Energy Environ. Sci.* **2014**, *7*, 2448.
[12] H. Zhou, Q. Chen, G. Li, S. Luo, T. Song, H.-S. Duan, Z. Hong, J. You, Y. Liu, Y. Yang, *Science.* **2014**, *345*, 542.
[13] M. Grätzel, *Nat. Mater.* **2014**, *13*, 838.
[14] Z. H. Bakr, Q. Wali, A. Fakharuddin, L. Schmidt-Mende, T. M. Brown, R. Jose, *Nano Energy* **2017**, *34*, 271.
[15] N. J. Jeon, J. H. Noh, W. S. Yang, Y. C. Kim, S. Ryu, J. Seo, S. Il Seok, *Nature* **2015**, *517*, 476.
[16] B. X. Chen, W. G. Li, H. S. Rao, Y. F. Xu, D. Bin Kuang, C. Y. Su, *Nano Energy* **2017**, *34*, 264.
[17] N. Pellet, P. Gao, G. Gregori, T. Y. Yang, M. K. Nazeeruddin, J. Maier, M. Grätzel, *Angew. Chemie - Int. Ed.* **2014**, *53*, 3151.
[18] C. S. Ponseca, T. J. Savenije, M. Abdellah, K. Zheng, A. Yartsev, T. Pascher, T. Harlang, P. Chabera, T. Pullerits, A. Stepanov, J. P. Wolf, V. Sundström, *J. Am. Chem. Soc.* **2014**, *136*, 5189.
[19] L. Meng, J. You, T.-F. Guo, Y. Yang, *Am. Chem. Soc.* **2015**, *49*, 155.
[20] NREL, “Photovoltaic Research,” can be found under https://www.nrel.gov/pv/assets/images/efficiency-chart.png, **2017**.
[21] S. Ameen, M. A. Rub, S. A. Kosa, K. A. Alamry, M. S. Akhtar, H. S. Shin, H. K. Seo, A. M. Asiri, M. K. Nazeeruddin, *ChemSusChem* **2016**, *9*, 10.
[22] J. P. Correa Baena, L. Steier, W. Tress, M. Saliba, S. Neutzner, T. Matsui, F. Giordano, T. J. Jacobsson, A. R. Srimath Kandada, S. M. Zakeeruddin, A. Petrozza, A. Abate, M. K. Nazeeruddin, M. Grätzel, A. Hagfeldt, *Energy Environ. Sci.* **2015**, *8*, 2928.
[23] T. S. Sherkar, C. Momblona, L. Gil-Escrig, J. Ávila, M. Sessolo, H. J. Bolink, L. J. A. Koster, *ACS Energy Lett.* **2017**, *2*, 1214.
[24] Z. Song, S. C. Watthage, A. B. Phillips, M. J. Heben, *J. Photonics Energy* **2016**, *6*, 22001.
[25] Y. Qin, M. A. Uddin, Y. Chen, B. Jang, K. Zhao, Z. Zheng, R. Yu, T. J. Shin, H. Y. Woo, J. Hou, *Adv. Mater.* **2016**, *28*, 9416.
[26] X. Liu, F. Kong, S. Jin, W. Chen, T. Yu, T. Hayat, A. Alsaedi, H. Wang, Z. Tan, J. Chen, S. Dai, *ACS Appl. Mater. Interfaces* **2017**, *9*, 27657.
[27] H. Xi, S. Tang, X. Ma, J. Chang, D. Chen, Z. Lin, P. Zhong, H. Wang, C. Zhang, *ACS Omega* **2017**, *2*, 326.
[28] D. Bi, W. Tress, M. I. Dar, P. Gao, J. Luo, C. Renevier, K. Schenk, A. Abate, F. Giordano, J.-P. Correa Baena, J.-D. Decoppet, S. M. Zakeeruddin, M. K. Nazeeruddin, M. Grätzel, A. Hagfeldt, *Sci. Adv.* **2016**, *2*,7.
[29] O. Wiranwetchayan, S. Promnopas, T. Thongtem, A. Chaipanich, S. Thongtem, *Surf. Coatings Technol.* **2017**, *326*, 310.
[30] S. Honsberg, Christina Bowden, “PVeducation.org,” can be found under http://www.pveducation.org/, *Accessed on 4 November.*
[31] B. Qi, J. Wang, *Phys. Chem. Chem. Phys.* **2013**, *15*, 8972.
[32] The University of Sheffield, “The X-ray Diffraction Small Research Facility: What is XRD?,” **2017**.
[33] W. Yan, H. Rao, C. Wei, Z. Liu, Z. Bian, H. Xin, W. Huang, *Nano Energy* **2017**, *35*, 62.
[34] H. Tan, A. Jain, O. Voznyy, X. Lan, F. P. García de Arquer, J. Z. Fan, R. Quintero-Bermudez, M. Yuan, B. Zhang, Y. Zhao, F. Fan, P. Li, L. N. Quan, Y. Zhao, Z.-H. Lu, Z. Yang, S. Hoogland, E. H. Sargent, *Science.* **2017**, *355*, 722.
[35] T. M. A. Kojima, K. Teshima, Y. Shirai, *J. Am. Chem. Soc.* **2006.** *131*, 6050.
[36] J. Im, C. Lee, J. Lee, S. Park, N. Park, *Nanoscale.* **2011.** 3, 4088.
[37] M. J. Spiers, University of Groningen. *Device Physics of Colloidal Quantum Dot Solar Cells* RUG, **2017**.